

Showcasing research from Professor Gaharwar's laboratory, Department of Biomedical Engineering, Texas A&M University, United States.

Superhydrophobic states of 2D nanomaterials controlled by atomic defects can modulate cell adhesion

A new concept to control the wetting characteristics by modulating atomic defects in 2D-nanomaterials is introduced. This work shed new light on the role of atomic vacancies on wetting characteristic that can be leveraged to develop superhydrophobic surfaces for biomedical applications.

### As featured in:



See Manish K. Jaiswal,  
Akhilesh K. Gaharwar *et al.*,  
*Chem. Commun.*, 2019, **55**, 8772.



Cite this: *Chem. Commun.*, 2019, 55, 8772

Received 21st January 2019,  
Accepted 11th May 2019

DOI: 10.1039/c9cc00547a

rsc.li/chemcomm

## Superhydrophobic states of 2D nanomaterials controlled by atomic defects can modulate cell adhesion†

Manish K. Jaiswal,<sup>a</sup> Kanwar Abhay Singh,<sup>a</sup> Giriraj Lokhande<sup>a</sup> and Akhilesh K. Gaharwar<sup>abc</sup>

**We introduced a new concept to the control of wetting characteristics by modulating the degree of atomic defects of two-dimensional transition metal dichalcogenide nanoassemblies of molybdenum disulfide. This work shed new light on the role of atomic vacancies on wetting characteristic that can be leveraged to develop a new class of superhydrophobic surfaces for various applications without altering their topography.**

Superhydrophobic materials are used extensively in bioelectronics, medical, and self-cleaning devices. These superhydrophobic properties rely on altering topological features such as surface roughness and surface energy. For instance, microstructural features with grooves filled with air-packets govern the wetting behavior of microengineered superhydrophobic surfaces.<sup>1</sup> Such behavior has been explained by Cassie–Baxter wetting theory, where liquid droplets make contact only with tips of the grooves, and intact air-packets support the spherical shape of the droplet to provide superhydrophobic properties.<sup>2,3</sup> These methods involve a cumbersome fabrication approach and cannot be applied to biosensing, lab-on-a-chip, blood-repellent, anti-fouling, and self-cleaning applications, which demand a non-textured approach to achieve a superhydrophobic state.

Two-dimensional (2D) nanomaterials have received considerable attention due to high degree of structural anisotropy and chemical functionality.<sup>4–7</sup> For example, 2D transition metal dichalcogenide (TMD) nanosheets have been investigated for nanoelectronics, optical sensors, renewable energy sources, catalysis, and lubrication.<sup>8–10</sup> In particular, 2D molybdenum disulfide (MoS<sub>2</sub>) has been explored in nanoelectronics<sup>9,11</sup> and as a photothermal agent<sup>12–14</sup> due to its tunable band gap. The

atomic defects present on the lattice plane of MoS<sub>2</sub> provide an active site for various applications, including catalyst and chemical conjugations.<sup>10,15</sup> More recently, hierarchical nanoassemblies of defect-rich MoS<sub>2</sub> have been shown to improve the performance of lithium ion storage batteries by 20-fold compared with traditional monolayers of MoS<sub>2</sub>,<sup>16–19</sup> and can be used to form hydrogels using polymeric binders *via* metal-click chemistry.<sup>20</sup> MoS<sub>2</sub> is cytocompatible and degrades in an *in vitro* microenvironment and, thus, has been explored for various biomedical applications.<sup>21</sup>

In the past few years, the superhydrophobic characteristics of 2D nanomaterials such as graphene,<sup>22</sup> boron nitride,<sup>23</sup> tungsten disulfide (WS<sub>2</sub>),<sup>24</sup> and MoS<sub>2</sub><sup>25</sup> have been reported. The wetting characteristics of these 2D nanomaterials are attributed mostly to the surface roughness or deposition of air-borne hydrocarbons which, ultimately, reduce the surface activity.<sup>25,26</sup> Atomic defects that can be incorporated into 2D nanomaterials during the synthetic process have not been investigated but which could provide a facile approach to tune the wetting characteristics.

Here, we report the tunable wetting behavior of defect-rich MoS<sub>2</sub> *via* modulating atomic vacancies. Specifically, we demonstrated that MoS<sub>2</sub> with a low degree of atomic defects resulted in superhydrophobic behavior (contact angle > 150°), whereas a high degree of atomic defects resulted in superhydrophilic properties (contact angle ~ 0). The wetting properties controlled by atomic vacancies displayed minimum hysteresis of the contact angle, indicating that the superhydrophobic behavior was independent of the amount of energy dissipated during wetting and dewetting. The superhydrophobic MoS<sub>2</sub> could be coated on various substrates (glass, silica, rubber and paper), thereby indicating high versatility for surface-coating applications.

MoS<sub>2</sub> nanoassemblies with predefined atomic defects were synthesized by modulating the ratio of precursors of molybdenum (hexaammonium heptamolybdate):sulfur (thiourea) (1:1, 1:2, 1:4 and 1:6) (see ESI†). The defect-rich MoS<sub>2</sub> lattice had hexagonal crystallographic arrangements of Mo and S atoms (Fig. 1a). Depending on the precursor ratio (Mo:S), the number of atomic

<sup>a</sup> Department of Biomedical Engineering, Texas A&M University, College Station, TX-77843, USA. E-mail: gaharwar@tamu.edu, manish@tamu.edu

<sup>b</sup> Department of Biomedical Engineering, Texas A&M University, College Station, TX-77843, USA

<sup>c</sup> Center for Remote Health Technologies & Systems, Texas A&M University, College Station, TX-77843, USA

† Electronic supplementary information (ESI) available: Experimental methods and materials characterizations are detailed. See DOI: 10.1039/c9cc00547a



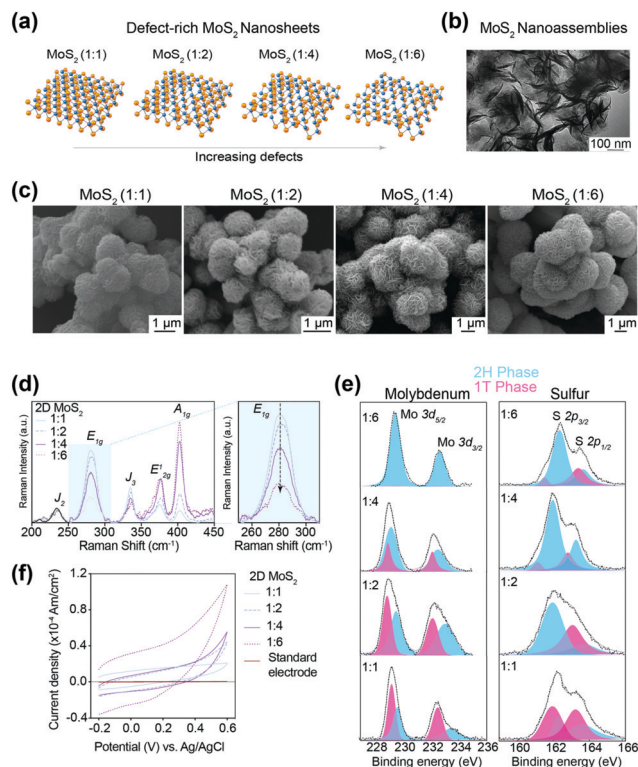


**Fig. 1** Defect-rich nanoassembly of 2D MoS<sub>2</sub> sheets. (a) Changing the ratio of molybdenum : sulfur precursors led to the formation of MoS<sub>2</sub> with different degrees of atomic vacancies. (b) TEM image confirmed the order of individual sheets into nanoassemblies. (c) SEM image shows a “flower”-like morphology of nanoassemblies of typical size 1.5–3 μm. No significant change in size or shape was observed due to changes in atomic vacancies for MoS<sub>2</sub> (1 : 1, 1 : 2, 1 : 4 and 1 : 6 samples). (d) Raman spectra confirmed 2H to be the dominant phase with a partial presence of 1T-phase formation. The vibrations of in-plane S atoms confirmed that a highly ordered and pronounced 2H phase was present with increasing amounts of the sulfur precursor. (e) XPS showing the core-level binding energies of Mo and S atoms for MoS<sub>2</sub> samples. (f) Cyclic voltammetry verified the increased defect densities with increasing amounts of the sulfur precursor, thus confirming 1 : 1 with least atomic vacancies and 1 : 6 with maximum atomic vacancies.

defects could be modulated from sample 1:1 to 1:6. The transmission electron microscopy (TEM) image of typical defect-rich MoS<sub>2</sub> shows the nanoassembly of individual 2D sheets (Fig. 1b). The scanning electron microscopy (SEM) images of MoS<sub>2</sub> samples with different ratios of Mo and S demonstrated a well-segregated “flower-like” hierarchical architecture (Fig. 1c). The average size of nanoassemblies was 1.5–3 μm. A significant effect of atomic defects on the size of nanoassemblies was not observed (Fig. S1, ESI<sup>†</sup>).

In 2D MoS<sub>2</sub>, a layer of Mo (oxidative state, 4+) atoms was held between two layers of S (oxidative state, 2-) atoms. Two MoS<sub>2</sub> layers interacted with each other *via* short-range van der Waals interactions. The Mo atoms could have trigonal prismatic co-ordination with S atoms to result in hexagonal symmetry (2H phase) or octahedral co-ordination to result in tetragonal symmetry (1T phase). The Raman spectra showed the formation of a dominant 2H phase with partial presence of the 1T phase (Fig. 1d).

The characteristic E<sub>2g</sub><sup>1</sup> (in-plane vibration of two S atoms) and A<sub>1g</sub> (out-of-plane vibration of S atoms) occurred at ~375 cm<sup>-1</sup> and ~402 cm<sup>-1</sup>, respectively. The appearance of the E<sub>1g</sub> peak at 280 cm<sup>-1</sup> (which was due to the tetragonal symmetry of the lattice) indicated a metastable 1T phase besides the dominant 2H phase in MoS<sub>2</sub> samples, which was likely due to ammonium cations released during synthesis.<sup>27</sup> Furthermore, as expected, a simultaneous attenuation in the intensity of the E<sub>1g</sub> peak accompanied with gradual amplification in E<sub>2g</sub><sup>1</sup> and A<sub>1g</sub> from sample 1 : 1 to sample 1 : 6 demonstrated the formation of a highly ordered 2H phase with an increase in thiourea concentration. The observation in Raman spectra was corroborated further with X-ray photoelectron spectroscopy (XPS) for the core-level binding energies of Mo and S atoms for MoS<sub>2</sub> samples (1 : 1, 1 : 2, 1 : 4 and 1 : 6) (Fig. 1e). The presence of the 1T phase (tetragonal symmetry) was dominated by the 2H phase (hexagonal symmetry), as represented by blue curves with increments in the sulfur precursor (thiourea content) from 1 : 1 through 1 : 6. These results corroborated the findings of Raman spectroscopy. The specific BE for the 1T-phase Mo was (3d<sub>5/2</sub>) 229.2 and (3d<sub>3/2</sub>) 232.4 eV, and for S was (2p<sub>3/2</sub>) 161.9 and (2p<sub>1/2</sub>) 163.1 eV. The corresponding BE for the 2H phase was slightly higher for Mo (229.6 and 233.3 eV) and S (162.2 eV and 163.5 eV), respectively.

The number of atomic vacancies for 2D MoS<sub>2</sub> was determined with cyclic voltammetry *via* expanded *J/V* (current density *vs.* potential) curves (Fig. 1f). An increase in the sulfur precursor (thiourea) resulted in an increase in the area under the *J/V* curve. The concentration of atomic defects increased with an increase in the Mo:S precursor ratio, 1 : 1 (~0.59 × 10<sup>2</sup> μM g<sup>-1</sup>), 1 : 2 (~0.72 × 10<sup>2</sup> μM g<sup>-1</sup>), 1 : 4 (~0.80 × 10<sup>2</sup> μM g<sup>-1</sup>) and 1 : 6 (~2.1 × 10<sup>2</sup> μM g<sup>-1</sup>) (see ESI<sup>†</sup> for details).

The effect of atomic vacancy on wetting characteristics was evaluated by determining the contact angle of water and polar/non-polar organic solvents on MoS<sub>2</sub>-coated surfaces. To determine wetting characteristics, the water contact angle on a MoS<sub>2</sub> (1 : 1, 1 : 2, 1 : 4 and 1 : 6)-coated glass substrate was evaluated (Fig. 2a). The highest contact angle was observed for sample 1 : 1 (157.5 ± 5.2°), which decreased gradually for sample 1 : 2 (137.6 ± 2.0°), sample 1 : 4 (23.7 ± 10.0°) and sample 1 : 6 (3.6 ± 3.0°), thus causing the surface to become superhydrophilic. The associated liquid-droplet images are shown on top of the bar graph. As expected, the droplet shape was spherical for 1 : 1, indicating superhydrophobic characteristics. As the ratio of sulfur precursor increased during MoS<sub>2</sub> synthesis, the water droplet became oblate (1 : 2) and eventually spread (1 : 4) and adsorbed (1 : 6) onto the coated surface, thereby suggesting atomic defect-dependent wetting behavior.

To further verify superhydrophobic characteristics, a rectangular pattern (2 cm × 1 cm) covering the boundary area using MoS<sub>2</sub> (1 : 1) on the glass slide was filled with 1 mL of water (Fig. 2b). The uniform coating of MoS<sub>2</sub> (1 : 1) on the glass substrate was verified using SEM. The rectangular pattern (thickness, 0.5 μm) could hold 10-fold water molecules (height, 5 μm) due to its superhydrophobic characteristics. Even after it was subjected to manual shaking, the movement of water was confined within the rectangle area due to the hydrophobic nature of the MoS<sub>2</sub> (see ESI<sup>†</sup>, Video V1). In addition, a water droplet was allowed to roll-down



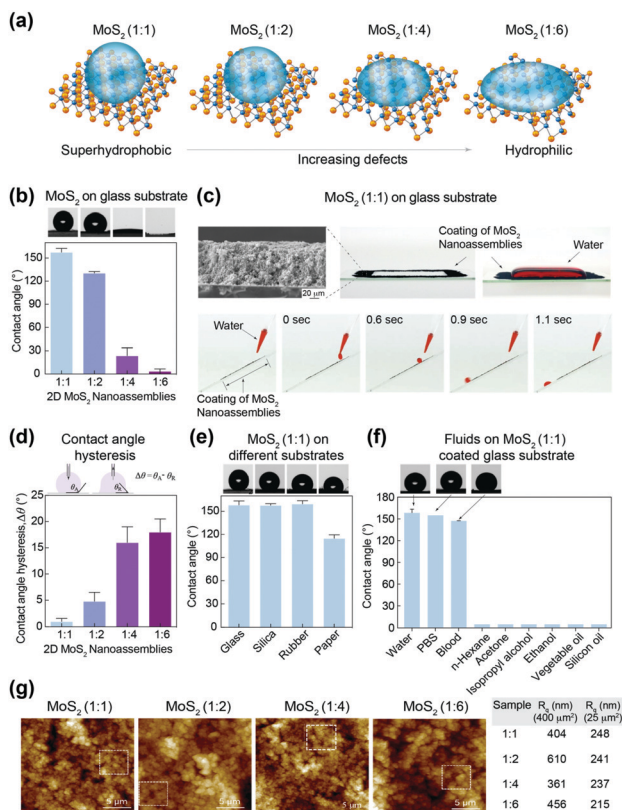


**Fig. 2** Wetting characteristics of defect-rich  $\text{MoS}_2$  nanoassemblies. (a) Wetting characteristics are controlled by atomic defects. (b) The contact-angle measurements of  $\text{MoS}_2$  (1:1, 1:2, 1:4, and 1:6)-coated glass slides exhibited superhydrophobic-to-superhydrophilic transition. (c) A  $\text{MoS}_2$  (1:1)-coated rectangular area confined the water droplet without spilling. The water droplets (red) rolled down on the  $\text{MoS}_2$  (1:1)-coated slanted surface without being adsorbed. (d)  $\text{MoS}_2$  (1:1)- and  $\text{MoS}_2$  (1:2)-coated surfaces showed low hysteresis of the contact angle. (e)  $\text{MoS}_2$  (1:1) coated on glass, silica, rubber and paper retained its superhydrophobic characteristics. (f) The superhydrophobic behavior of a  $\text{MoS}_2$  (1:1)-coated surface was observed for water, PBS and blood, whereas an organic solvent was readily spread on the surface. (g) The roughness ( $R_q$ ) for all four  $\text{MoS}_2$  samples was analyzed by AFM for 400 and 25  $\mu\text{m}^2$  imaging areas. The values are presented in the table.

a slanted glass slide coated with  $\text{MoS}_2$  (1:1) to investigate the superhydrophobic properties in dynamic conditions. The water droplet (red) rolled down without being adsorbed over the surface and remained intact (spherical shape) during rolling. Hence,  $\text{MoS}_2$  (1:1) could be used for various coating applications (Fig. 2b and c; see ESI,† Video V2).

The wetting behavior of a  $\text{MoS}_2$ -coated surface can be understood in terms of the interfacial tension ( $\gamma$ ) between the liquid and the coating as given by Young's equation,<sup>28</sup>  $\cos \theta = (\gamma_{\text{sa}} - \gamma_{\text{sl}})/\gamma_{\text{la}}$ , where  $\theta$  is the contact angle,  $\gamma_{\text{sl}}$  is the solid/liquid interfacial free energy,  $\gamma_{\text{sa}}$  is the solid surface free energy, and  $\gamma_{\text{la}}$  is the liquid surface free energy. As the Mo:S precursor ratio changed from 1:1 to 1:6, the interaction between the  $\text{MoS}_2$ -coated surface and water molecules increased due to the presence of defects owing to direct access of the Mo atomic plane, and could potentially form a molybdenum–water complex. This resulted in reduction of the interfacial tension between the liquid and substrate ( $\gamma_{\text{sl}}$ ) and

surface tensions ( $\gamma_{\text{sa}}$  and  $\gamma_{\text{la}}$ ) approached each other. This results in  $\theta$  tended to zero, thus causing the sample to become superhydrophilic.

The contact angle is often a function of whether the liquid is advancing or receding on the substrate.<sup>28</sup> To ascertain such possible behavior of the samples, the contact angle hysteresis ( $\Delta\theta$ ) was measured (which is essentially the difference between advancing ( $\theta_{\text{A}}$ ) and receding contact angles ( $\theta_{\text{R}}$ )). As expected,  $\Delta\theta$  was minimal for the  $\text{MoS}_2$  samples 1:1 ( $1 \pm 0.6^\circ$ ) and 1:2 ( $4.8 \pm 1.7^\circ$ ), indicating that their superhydrophobic character was independent of roughness or surface contamination (Fig. 2d). Higher  $\Delta\theta$  was observed for sample 1:4 ( $16 \pm 3^\circ$ ) and 1:6 ( $18 \pm 2.5^\circ$ ). The low  $\Delta\theta$  for  $\text{MoS}_2$  (1:1) indicated that the Cassi–Baxter wetting behavior of the liquid caused the droplets to roll-down in a spherical shape over the slightly slanted surface (see ESI†). Such superhydrophobic materials with small  $\Delta\theta$  are highly sought after for commercial applications (e.g., designing self-cleaning and spill-resistance coating materials for exterior glass and wind shields).

To further investigate the versatility of  $\text{MoS}_2$  (1:1) as a superhydrophobic coating, substrates such as silica, rubber and papers were coated with  $\text{MoS}_2$  (1:1) and the water contact angle determined (Fig. 2e). All the surfaces showed superhydrophobic characteristics: silica ( $157.8 \pm 5.2^\circ$ ), rubber ( $159.7 \pm 4.0^\circ$ ), and paper ( $115 \pm 4.7^\circ$ ). In addition, the contact angle for various biological fluids and organic solvents, including phosphate-buffered saline (PBS) (pH 7.4), whole blood, hexane, ethanol, isopropanol, fatty vegetable oil and silicone oil, were investigated (Fig. 2f). The contact angle for PBS ( $151.0 \pm 1.07^\circ$ ) and whole blood ( $147.2 \pm 0.41^\circ$ ) was similar to that of water. For glycerol ( $106.0 \pm 28.6^\circ$ ), silicone oil ( $16.4 \pm 2.5^\circ$ ) and other organic solvents ( $\sim 5^\circ$ ), the contact angle was lower due to enhanced interactions of the sulfur layer (from  $\text{MoS}_2$ ) with hydrocarbons, acetone and mild polar alcohols. Moreover, an aqueous solution of an amphiphile, such as sodium dodecyl sulfate (SDS), spread onto the  $\text{MoS}_2$  (1:1 and 1:6)-coated glass substrate.

To investigate the effect of surface roughness on wetting characteristics, topographical analysis was carried out using atomic force microscopy (AFM). The root-mean square value of roughness ( $R_q$ ) was calculated for an imaging area of 400 and 25  $\mu\text{m}^2$  for all samples (Fig. 2g). There was no significant difference in  $R_q$  (400–600 nm for 400  $\mu\text{m}^2$  and 220–250 nm for 25  $\mu\text{m}^2$ ) for different  $\text{MoS}_2$  (1:1 to 1:6) samples. This observation suggested that topographical features did not govern the hydrophobic character of  $\text{MoS}_2$ .

We investigated the adhesion of human mesenchymal stem cells (hMSCs) onto superhydrophobic (1:1) and superhydrophilic surfaces (1:6). High adhesion of hMSCs was observed on hydrophilic surfaces. Superhydrophobic surfaces of  $\text{MoS}_2$  (1:1) restricted adhesion of hMSCs compared with  $\text{MoS}_2$  (1:6) (Fig. 3a). To investigate the role of protein adsorption, we tested adhesion of hMSCs in the presence and absence of serum. We observed significantly higher adhesion of hMSCs in the presence of serum in both  $\text{MoS}_2$  surfaces (1:1 and 1:6). Energy-dispersive X-ray spectroscopy (EDS) mapping for C and N elements confirmed the higher adhesion of hMSCs on hydrophilic surfaces of  $\text{MoS}_2$  (1:6).



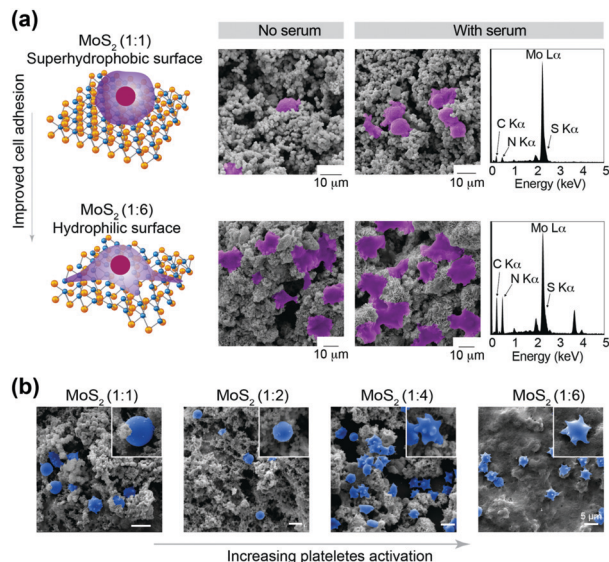


**Fig. 3** Cell-adhesion characteristics of defect-rich MoS<sub>2</sub> nanoassemblies. (a) Cellular adhesion on MoS<sub>2</sub>-coated substrates (1:1, hydrophobic) and (1:6, hydrophilic) in the presence and absence of serum proteins. The false-color SEM images show adherent cells in purple. Energy-dispersive X-ray spectroscopy (EDS) profile showing stronger peaks of C and N, which further confirmed higher cell adhesion for hydrophilic substrates regardless of serum addition. (b) Adhesion and activation of platelets on MoS<sub>2</sub>-coated substrates. The morphological changes of platelets shown using the false blue color in SEM images demonstrated hydrophobicity-controlled activation of platelets.

However, we did not observe a significant change in protein adsorption on MoS<sub>2</sub> surfaces (1:1 and 1:6). We further evaluated the effect of wetting characteristics on platelet activation. The adhesion and activation of platelets was done using bovine blood on MoS<sub>2</sub> surfaces (1:1 through 1:6) (Fig. 3b). The hydrophilic nature of the surface promoted platelet activation.

In summary, we introduced a new concept to control the wetting characteristics of 2D nanomaterials by modulating the degree of atomic defects. Specifically, we synthesized superhydrophobic 2D MoS<sub>2</sub> and demonstrated that atomic defects dictated hydrophilic-to-hydrophobic transition. The highest contact angle was observed for MoS<sub>2</sub> with a Mo:S precursor ratio of 1:1 ( $157.5 \pm 5.2^\circ$ ), which decreased gradually for 1:2 ( $137.6 \pm 2.0^\circ$ ), 1:4 ( $23.7 \pm 10.0^\circ$ ) and 1:6 ( $3.6 \pm 3.0^\circ$ ), thus causing the surface to become superhydrophilic. MoS<sub>2</sub> (1:1) could be coated readily on glass, silica, rubber and paper and retain its superhydrophobic characteristics. Due to low  $\Delta\theta$ , superhydrophobic MoS<sub>2</sub> (1:1) could be used for biosensing, lab-on-a-chip, blood-repellent, anti-fouling, and self-cleaning applications, which demand a non-textured approach to achieve a superhydrophobic state. The wetting characteristics of the MoS<sub>2</sub> surface directly influence cell-adhesion characteristics that can be leveraged for biomedical applications.

We thank James L. Gentry for the synthesis and deposition of defect-rich MoS<sub>2</sub> films and preparing supporting videos. Dr James K. Carrow and Dr Jagriti Gupta (IIT Bombay) assisted in contact-angle measurements and cyclic voltammetry, respectively.

The research reported in this publication was supported by the National Institutes of Health (NIH) Director's New Innovator Award (DP2 EB026265) by National Institute of Biomedical Imaging and Bioengineering (NIBIB).

## Conflicts of interest

There are no conflicts to declare.

## Notes and references

- V. Jokinen, E. Kankuri, S. Hoshian, S. Franssila and R. H. A. Ras, *Adv. Mater.*, 2018, **30**, 1705104.
- F.-M. Chang, S.-J. Hong, Y.-J. Sheng and H.-K. Tsao, *Appl. Phys. Lett.*, 2009, **95**, 064102.
- J. López-Cabrelles, S. Mañas-Valero, I. J. Vitorica-Yrezabal, P. J. Bereciartua, J. A. Rodríguez-Velamazán, J. C. Waerenborgh, B. J. C. Vieira, D. Davidovikj, P. G. Steeneken, H. S. J. van der Zant, G. Mínguez Espallargas and E. Coronado, *Nat. Chem.*, 2018, **10**, 1001–1007.
- D. Voiry, A. Goswami, R. Kappera, E. SilvaCecilia de Carvalho Castro, D. Kaplan, T. Fujita, M. Chen, T. Asefa and M. Chhowalla, *Nat. Chem.*, 2015, **7**, 45–49.
- V. Nicolosi, M. Chhowalla, M. G. Kanatzidis, M. S. Strano and J. N. Coleman, *Science*, 2013, **340**, 1226419.
- A. K. Gaharwar, L. M. Cross, C. W. Peak, K. Gold, J. K. Carrow, A. Brokesh and K. A. Singh, *Adv. Mater.*, 2019, DOI: 10.1002/adma.201900332.
- D. Chimene, D. Alge and A. K. Gaharwar, *Adv. Mater.*, 2015, **27**, 7261–7284.
- W. Li, X. Gao, D. Xiong, F. Wei, W.-G. Song, J. Xu and L. Liu, *Adv. Energy Mater.*, 2017, **7**, 1602579.
- M. Chhowalla, H. S. Shin, G. Eda, L.-J. Li, K. P. Loh and H. Zhang, *Nat. Chem.*, 2013, **5**, 263–275.
- T. Liu, S. Shi, C. Liang, S. Shen, L. Cheng, C. Wang, X. Song, S. Goel, T. E. Barnhart, W. Cai and Z. Liu, *ACS Nano*, 2015, **9**, 950–960.
- C. N. R. Rao, H. S. S. Ramakrishna Matte and U. Maitra, *Angew. Chem., Int. Ed.*, 2013, **52**, 13162–13185.
- W. Yin, L. Yan, J. Yu, G. Tian, L. Zhou, X. Zheng, X. Zhang, Y. Yong, J. Li, Z. Gu and Y. Zhao, *ACS Nano*, 2014, **8**, 6922–6933.
- M. Li, A. Zhao, K. Dong, W. Li, J. Ren and X. Qu, *Nano Res.*, 2015, **8**, 3216–3227.
- W. Yin, J. Yu, F. Lv, L. Yan, L. R. Zheng, Z. Gu and Y. Zhao, *ACS Nano*, 2016, **10**, 11000–11011.
- S. S. Chou, N. Sai, P. Lu, E. N. Coker, S. Liu, K. Artyushkova, T. S. Luk, B. Kaehr and C. J. Brinker, *Nat. Commun.*, 2015, **6**, 8311.
- G. Ye, Y. Gong, J. Lin, B. Li, Y. He, S. T. Pantelides, W. Zhou, R. Vajtai and P. M. Ajayan, *Nano Lett.*, 2016, **16**, 1097–1103.
- J. Xie, H. Zhang, S. Li, R. Wang, X. Sun, M. Zhou, J. Zhou, X. W. Lou and Y. Xie, *Adv. Mater.*, 2013, **25**, 5807–5813.
- Z. Wu, B. Li, Y. Xue, J. Li, Y. Zhang and F. Gao, *J. Mater. Chem. A*, 2015, **3**, 19445–19454.
- M. Wang, G. Li, H. Xu, Y. Qian and J. Yang, *ACS Appl. Mater. Interfaces*, 2013, **5**, 1003–1008.
- M. K. Jaiswal, J. K. Carrow, J. L. Gentry, J. Gupta, N. Altangerel, M. Scully and A. K. Gaharwar, *Adv. Mater.*, 2017, **29**, 1702037.
- R. Kurapati, L. Muzi, A. P. R. de Garibay, J. Russier, D. Voiry, I. A. Vacchi, M. Chhowalla and A. Bianco, *Adv. Funct. Mater.*, 2017, **27**, 1605176.
- J. Rafiee, M. A. Rafiee, Z. Z. Yu and N. Koratkar, *Adv. Mater.*, 2010, **22**, 2151–2154.
- W. Lei, D. Portehault, D. Liu, S. Qin and Y. Chen, *Nat. Commun.*, 2013, **4**, 1777.
- R. Xu, K. Zhang, X. Xu, M. He, F. Lu and B. Su, *Adv. Sci.*, 2018, **5**, 1700655.
- J. Choi, J. Mun, M. C. Wang, A. Ashraf, S.-W. Kang and S. Nam, *Nano Lett.*, 2017, **17**, 1756–1761.
- A. Kozbial, X. Gong, H. Liu and L. Li, *Langmuir*, 2015, **31**, 8429–8435.
- Y. Jiao, A. Mukhopadhyay, Y. Ma, L. Yang, A. M. Hafez and H. Zhu, *Adv. Energy Mater.*, 2018, **8**, 1702779.
- F.-M. Chang, S.-J. Hong, Y.-J. Sheng and H.-K. Tsao, *Appl. Phys. Lett.*, 2009, **95**, 064102.

